AGU PUBLICATIONS

Geophysical Research Letters

RESEARCH LETTER
10.1002/2014GL061959

Key Points:
- Geothermal energy production causes surface subsidence and crustal stressing
- Production at CPGF generates positive Coulomb stresses in EMC rupture zone
- Anthropogenic stresses exceed the tectonic loading rate at EMC hypocenter

Supporting Information:
- Readme
- Figure S1
- Figure S2
- Figure S3
- Figure S4
- Figure S5
- Table S1
- Text S1

Correspondence to:
D. T. Trugman,
dtrugman@ucsd.edu

Citation:
Trugman, D. T., A. A. Borsa, and D. T. Sandwell (2014), Did stresses from the Cerro Prieto Geothermal Field influence the El Mayor-Cucapah rupture sequence?, *Geophys. Res. Lett.*, *41*, doi:10.1002/2014GL061959.

Received 20 SEP 2014
Accepted 1 DEC 2014
Accepted article online 2 DEC 2014

Did stresses from the Cerro Prieto Geothermal Field influence the El Mayor-Cucapah rupture sequence?

Daniel T. Trugman[1], Adrian A. Borsa[1], and David T. Sandwell[1]

[1]Institute for Geophysics and Planetary Physics, Scripps Institution of Oceanography, San Diego, California, USA

Abstract The M_w 7.2 El Mayor-Cucapah (EMC) earthquake ruptured a complex fault system in northern Baja California that was previously considered inactive. The Cerro Prieto Geothermal Field (CPGF), site of the world's second largest geothermal power plant, is located approximately 15 km to the northeast of the EMC hypocenter. We investigate whether anthropogenic fluid extraction at the CPGF caused a significant perturbation to the stress field in the EMC rupture zone. We use Advanced Land Observing Satellite interferometric synthetic aperture radar data to develop a laterally heterogeneous model of fluid extraction at the CPGF and estimate that this extraction generates positive Coulomb stressing rates of order 15 kPa/yr near the EMC hypocenter, a value which exceeds the local tectonic stressing rate. Although we cannot definitively conclude that production at the CPGF triggered the EMC earthquake, its influence on the local stress field is substantial and should not be neglected in local seismic hazard assessments.

1. Introduction

The southern edge of the Pacific-North America plate boundary cuts directly through the Valle de Mexicali in northwestern Baja California. This region is part of a broad zone of tectonic deformation characterized by subparallel dextral faults that connect the spreading centers of the Gulf of California to the south with the San Andreas and San Jacinto Faults to the north. Much of the right-lateral plate motion in the region is accommodated on the nearby Cerro Prieto and Imperial faults, each slipping at an estimated rate of 40 mm/yr [*Bennett et al.*, 1996; *Atwater and Stock*, 1998]. The 2010 El Mayor-Cucapah (EMC) earthquake itself occurred to the west of these main plate boundary faults (Figure 1) but to the east of the Laguna Salada Fault, which hosted an M_w 7.1 earthquake in 1892 [*Fletcher and Spelz*, 2009]. Instead, the EMC event ruptured the Borrego and Pescadores Faults in the Sierra Cucapah to the north of its hypocenter, and the Indiviso fault to its south [*Wei et al.*, 2011]. The northern faults had been mapped prior to EMC event [*Barnard*, 1968; *Fletcher and Spelz*, 2009] but were presumed to slip at much lower rates than the adjacent plate boundary faults and show little evidence of Holocene faulting [*Fletcher et al.*, 2014]. The Indiviso Fault was previously unmapped, as it is buried beneath Colorado River Delta sediments.

The EMC earthquake was the largest in the region since the 1992 Landers earthquake [*Sieh*, 1993]. It resulted in the deaths of four people, injured hundreds of others, and triggered widespread landslides and liquefaction. Yet the faults responsible for this damage were previously thought to contribute negligibly to the regional seismic hazard [*Bennett et al.*, 1996; *Fletcher et al.*, 2014]. In this study, we consider whether the extraction of fluids and heat related to energy production at the nearby Cerro Prieto Geothermal Field (CPGF) could have played a role in stressing these faults and initiating the EMC event, or sustaining its prolonged rupture.

The CPGF is the second largest geothermal power plant in the world [*Ocampo-Díaz et al.*, 2005; *CFE*, 2006; *Sarychikhina et al.*, 2011] and is located approximately 15 km to the northeast of the EMC hypocenter, in the extensional step over between the Cerro Prieto and Imperial Faults (Figure 1). Geothermal energy production and the associated fluid extraction have caused surface subsidence in the vicinity of the CPGF at previously reported rates of 10–15 cm/yr [*Glowacka et al.*, 2005, 2010; *Sarychikhina et al.*, 2011].

The extraction process, in turn, perturbs the regional crustal stress field and has been investigated for its possible role in triggering large, nearby earthquakes in the recent past [*Glowacka and Nava*, 1996]. The central aim of this study is to estimate the stressing rate on the faults that ruptured in the EMC earthquake due to extraction at the CPGF. We begin by using interferometric synthetic aperture radar (InSAR) data from Advanced Land Observing Satellite (ALOS) tracks recorded from 2006 to 2009 to constrain the magnitude

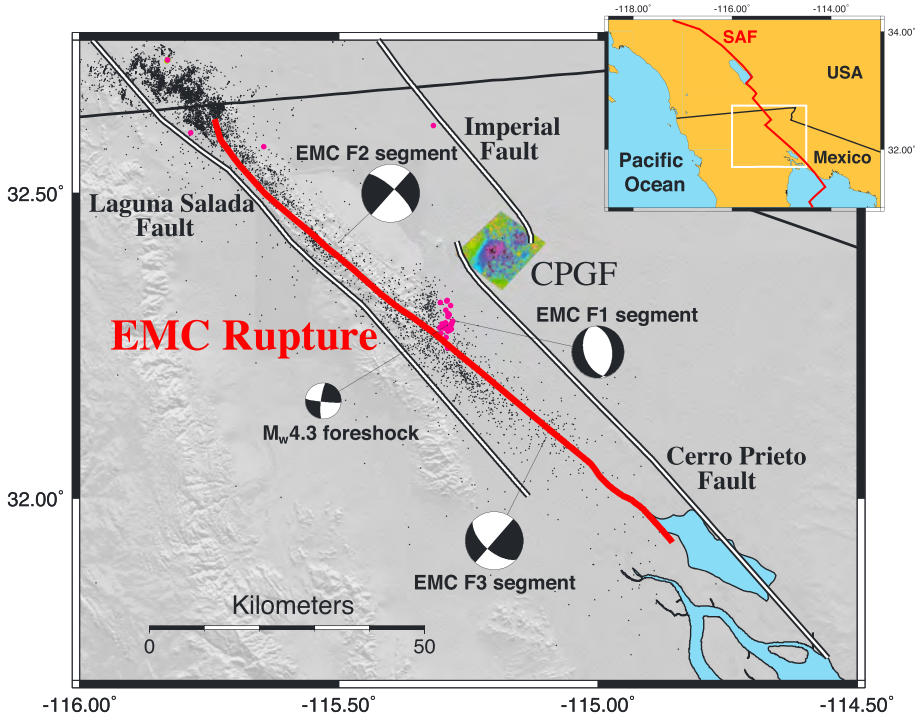

Figure 1. Map of the El Mayor-Cucapah (EMC) study region. The major regional faults (Laguna Salada, Cerro Prieto, and Imperial) are outlined in white, with the EMC earthquake rupture trace [*Wei et al.*, 2011] outlined in red. Pink circles show epicenters of the events in the foreshock sequence preceding the EMC rupture, with moment tensors for the M_w 4.3 foreshock, and F1, F2, and F3 EMC subevents, shown for reference. Black dots indicate aftershock seismicity in the 30 days following the EMC event. All seismic events in the figure are derived from the Hauksson-Shearer waveform relocated earthquake catalog [*Hauksson et al.*, 2012]. Inset: location of the study region (white box) within northern Mexico and southern California. The San Andreas Fault boundary between the Pacific and North American Plates is marked in red.

and spatial extent of anthropogenic subsidence at the CPGF. We then model the complex pattern of fluid extraction and recharge at the CPGF as a distribution of Mogi-source spherical pressure cavities, using the observed InSAR surface deformation data in a regularized inversion scheme to estimate the source intensities. With this extraction model in hand, we compute the Coulomb stressing rate on the sequence of faults that ruptured during the EMC event and compare this stressing rate to the stressing rate caused by deep, interseismic fault slip on the major regional faults. We find that extraction at the CPGF imparts positive Coulomb stresses of order +15 kPa/yr on the faults involved in the EMC rupture sequence. Conversely, tectonic loading from other regional faults imparts a negative Coulomb stress of around −8 kPa/yr in this same location.

2. Subsidence Measurements at the Cerro Prieto Geothermal Field

The Cerro Prieto Geothermal Field (CPGF) is located in the Mexicali Valley of northern Baja California. It is one of four major geothermal fields in the Salton Trough tectonic province (the others being the Salton Sea, East Mesa, and Heber geothermal fields, all in the United States). The CPGF has been in continuous operation by the Comisión Federal de Electricidad since 1973, and with a current installed capacity of 820 MW, is the world's second largest geothermal energy source [*Ocampo-Díaz et al.*, 2005; *Sarychikhina et al.*, 2011].

Energy production at the CPGF requires extraction of hot water and steam from production wells with a mean depth of 2.7 km [*Gutiérrez-Negrín et al.*, 2010]. In 2008, a total fluid volume of 6.3×10^7 m^3 was extracted at the CPGF, a value typical of the published extraction rates since 1994 [*Glowacka et al.*, 2005; *Gutiérrez-Negrín et al.*, 2010]. While approximately 30% of the extracted fluid is reinjected on site [*Gutiérrez-Negrín et al.*, 2010], and nearly twice this amount is naturally recharged from the surrounding aquifers [*Glowacka et al.*, 2005], there is a net loss of fluids in the production zone that causes the Earth's surface to subside. Surface subsidence at the CPGF is well established: first, with leveling surveys dating back to 1977 and more recently using interferometric

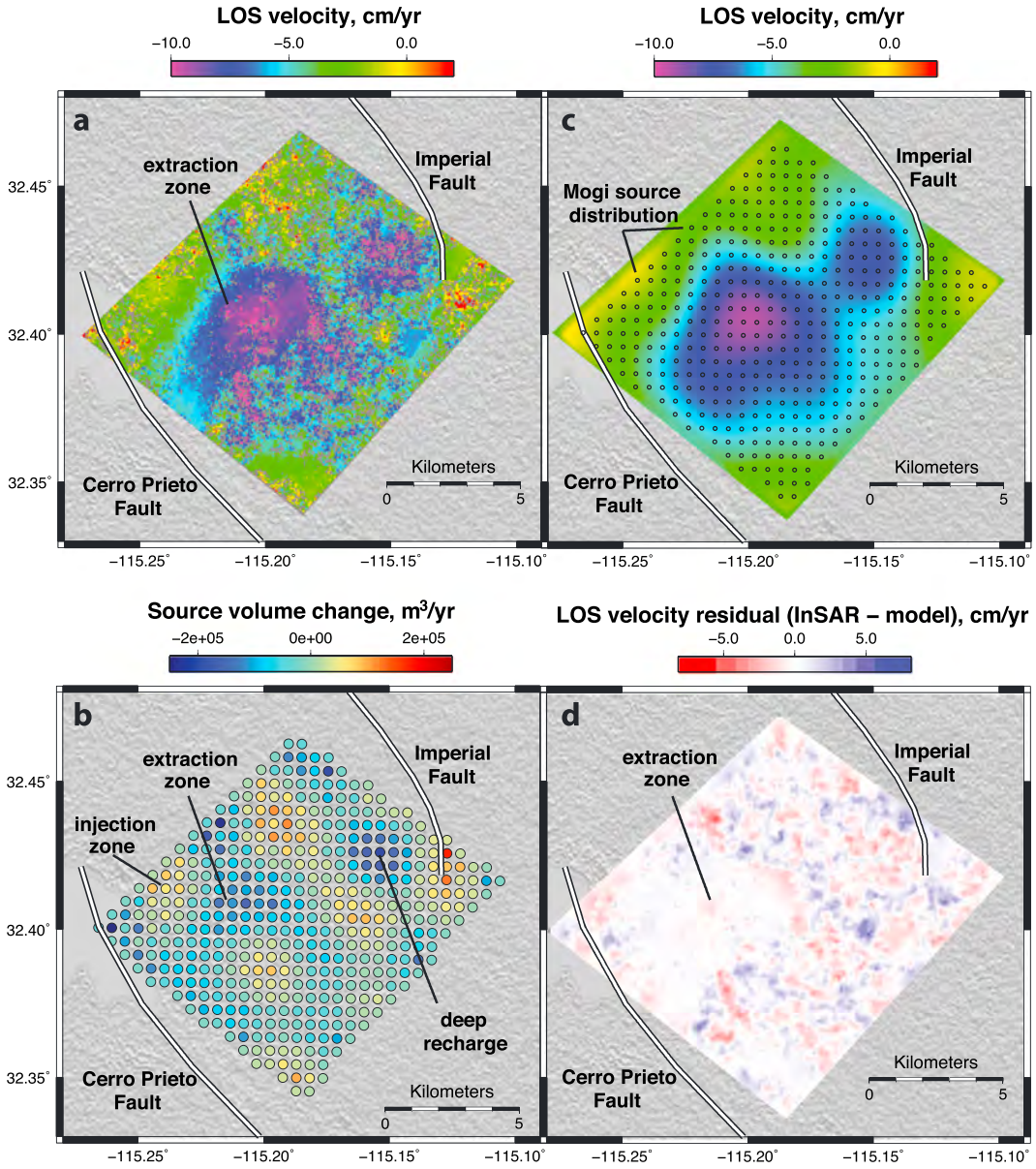

Figure 2. Subsidence at the Cerro Prieto Geothermal Field (CPGF). (a) InSAR image of the line-of-site (LOS) surface velocity field, made from stacking unwrapped ALOS interferograms from 2006 to 2009. Pixels with correlation < 0.1 are masked in the image. Negative velocities (blue) imply subsidence. The maximum vertical subsidence rate in the CPGF energy production site is ~ 14 cm/yr. (b) Preferred Mogi source distribution fluid extraction model derived from a regularized, least squares inversion of the InSAR LOS velocity field. Each Mogi source is color coded by its rate of volume change (m^3/yr). The integrated volume change over the source distribution is -9.0×10^6 m^3/yr**. (c)** LOS surface velocity field from our preferred Mogi source distribution fluid extraction model. Source locations are marked as open circles. The color scale and region are identical to Figure 2a. **(d)** Residual velocity field (InSAR model). Our preferred model provides a variance reduction of 69% on the observed InSAR data.

synthetic aperture radar (InSAR) techniques [*Carnec and Fabriol*, 1999; *Hanssen*, 2001; *Glowacka et al*., 2005]. These studies estimated a vertical subsidence rate at Cerro Prieto of 12 cm/yr, 90–95% of which is directly caused by fluid extraction at the CPGF [*Sarychikhina et al*., 2011].

We augment these previous observations with Advanced Land Observing Satellite (ALOS) InSAR data acquired from August 2006–January 2009 to study in detail the surface subsidence immediately preceding the EMC event. After initial processing of 23 InSAR images of the study region (see Text S1 in the supporting

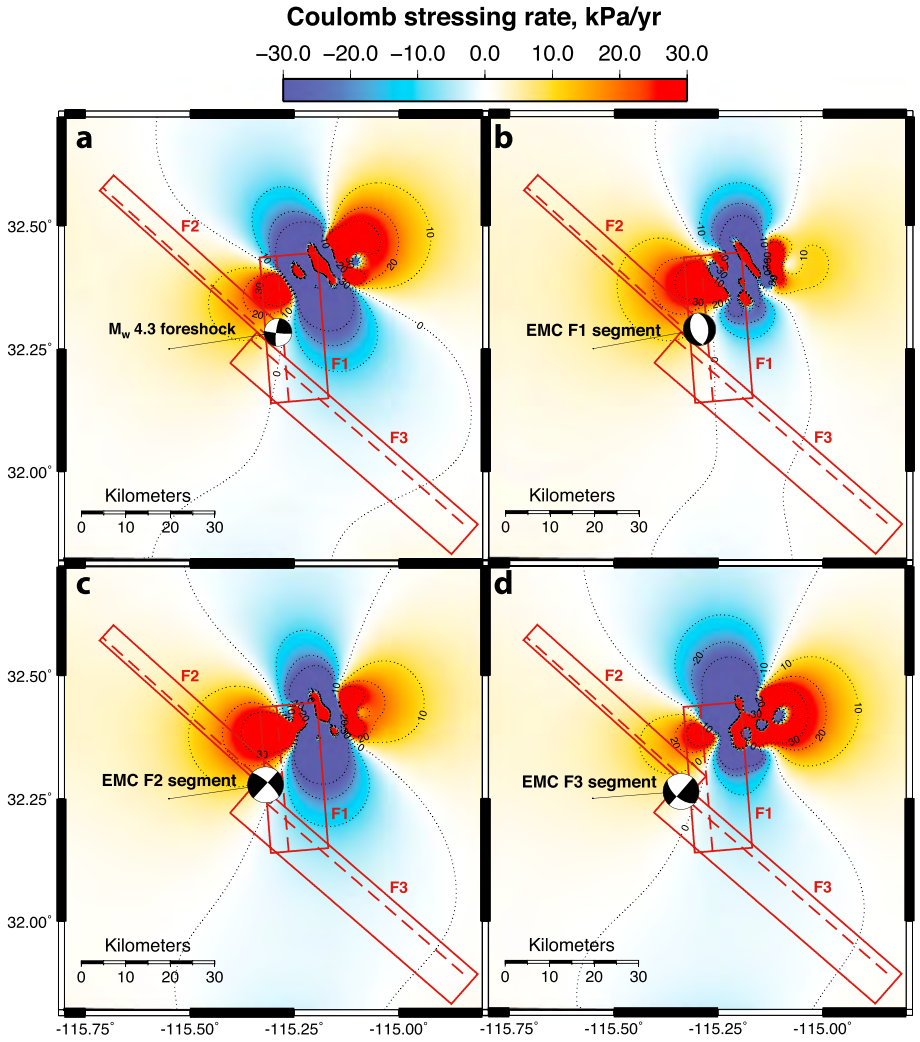

Figure 3. Coulomb stressing rates in the El Mayor-Cucapah (EMC) rupture zone due to fluid extraction at the Cerro Prieto Geothermal Field (CPGF). The F1, F2, and F3 subevent fault planes [*Wei et al.*, 2011] are shown for reference, with the assumed hypocentral depth of 5 km marked with a red dashed line. The color scale ranges from −30 to 30 kPa/yr, with contours displayed in increments of 10 kPa/yr. Coulomb stressing rate at 5 km depth is plotted for the fault geometries of **(a)** the M_w 4.3 foreshock (strike = 187°, dip = 79°, rake = 5°), **(b)** the F1 EMC subevent (strike = 355°, dip = 45°, rake = −80°), **(c)** the F2 EMC subevent (strike = 312°, dip = 75°, rake = −180°), and **(d)** the F3 EMC subevent (strike = 131°, dip = 60°, rake = −180°).

information for details), we stacked the two highest quality, phase-unwrapped [*Chen and Zebker*, 2001] interferograms to estimate the line-of-site (LOS) surface velocity field near the Cerro Prieto Geothermal Field (Figure 2a).

We estimate a maximum vertical subsidence rate of 14 cm/yr in the CPGF production zone, comparable to the findings of previous studies [*Sarychikhina et al.*, 2011]. This subsidence is almost entirely anthropogenic in origin, as local tectonics (i.e., deformation due to the position of the CPGF in an extensional step over) can account for at most 5% of the observed subsidence rate (Figure S1, see [*Glowacka et al.*, 2005] for a similar assessment). The spatial distribution of subsidence is characterized by two prominent lobes of deformation: one primary lobe situated directly above the energy production site, and a secondary lobe offset to the northeast that has been attributed to recharge of the main production area from a deep aquifer adjacent to the Imperial Fault [*Glowacka et al.*, 2005]. While this secondary lobe is still prominent in our ALOS InSAR data, it is somewhat diminished in magnitude relative to observations in earlier studies, perhaps indicating a decrease in recharge rate with time.

3. Fluid Extraction Model

The pronounced surface subsidence at the Cerro Prieto Geothermal Field is a product of a volume change at depth that is primarily caused by a net extraction of fluids, as thermoelastic effects are thought to contribute negligibly [*Mossop and Segall*, 1997]. In early studies linking surface deformation to geothermal fluid extraction [*Mossop and Segall*, 1997, 1999; *Carnec and Fabriol*, 1999], volumetric contraction was typically modeled as one or more point pressure cavity, or "Mogi" sources [*Mogi*, 1958]. More recent studies [*Sarychikhina*, 2003; *Glowacka et al*., 2005; *Sarychikhina et al*., 2011] have used site specific geologic constraints like fault boundaries to construct deformation models based on the superposition of large, rectangular, tensile (closing) cracks, while others [*Vasco et al*., 2002] subdivide the model domain into volume elements extending laterally and vertically to allow the model to assume any arbitrary shape.

We apply a hybrid approach in which we model the surface subsidence at the CPGF as the superposition of finely spaced Mogi pressure sources embedded in an elastic half space, applying constraints from independent information about the location and extent of the source region. For this study, we position the center of the source distribution in the production zone of the CPGF (−115.20°E, 32.1°N) and at the mean extraction depth of 2.7 km [*Lippmann et al*., 1991; *Gutiérrez-Negrín et al*., 2010]. We discretize the source distribution using a single horizontal layer with a grid spacing of 0.5 km in both lateral directions for a total of 436 evenly spaced sources. Although our approach does not allow us to distinguish between volumetric changes at different depths, it does allow the model to represent the horizontal variations in source intensity required to capture the complex spatial patterns of extraction, injection, and recharge beneath the CPGF.

For a single Mogi source at position (x_0, y_0, $z_0 < 0$) within an elastic half space (Poisson's ratio υ), the displacement vector (u_x, u_y, u_z) at surface position (x, y, $z = 0$), can be written as

$$\begin{pmatrix} u_x \\ u_y \\ u_z \end{pmatrix} = \frac{(1-\upsilon)\Delta V}{\pi} \begin{pmatrix} (x-x_0)/R^3 \\ (y-y_0)/R^3 \\ (-z_0)/R^3 \end{pmatrix} \quad (1)$$

where $R = \sqrt{(x-x_0)^2 + (y-y_0)^2 + (-z_0)^2}$ is the distance from the source to the surface observation point and ΔV is the associated volume change (i.e., the source intensity) [*Segall*, 2010]. Subsidence requires $\Delta V < 0$.

The observed surface deformation is the superposition of the deformation caused by each individual Mogi source in the distribution. We use the InSAR-derived LOS surface velocity field to perform a regularized, least squares inversion for the source volumes (Figure 2b; see Text S1 for details). Our preferred model's displacement field (Figure 2c) provides a 69% variance reduction (Figure 2d) on the observed InSAR data. We estimate a net rate of volumetric contraction of -9.0×10^6 m^3/yr. This estimated rate is insensitive to the details of the modeling assumptions (e.g., grid spacing and assumed depth) and inversion approach (e.g., choice of smoothing parameter) and is consistent both with the independent estimates of previous studies [*Sarychikhina et al*., 2011] and with available production data [*Gutiérrez-Negrín et al*., 2010].

4. Anthropogenic Stressing Rates Near the EMC Hypocenter

The EMC rupture sequence was complex [*Wei et al*., 2011], with slip likely initiating in a normal faulting subevent on a shallowly dipping fault plane (labeled F1 in Figures 1 and 3) striking almost due north. After a brief pause in moment release, the rupture jumped from the F1 fault plane onto NW striking right-lateral faults (see Figures 1 and 3) and ruptured bilaterally northward to the California border (fault plane F2) and southward to Gulf of California (fault plane F3). The M_w 7.2 EMC event was preceded by a vigorous foreshock sequence near the F1 hypocenter, culminating in a left-lateral, M_w 4.3 event less than 24 h prior to the main shock [*Hauksson et al*., 2011].

We use our model of CPGF fluid extraction to compute the anthropogenic stressing rate in the El Mayor-Cucapah rupture zone. Given a fault orientation and location, one can resolve the local stress tensor on that fault plane to compute the change in Coulomb stress:

$$\Delta\sigma_C = \Delta\tau + \mu'\Delta\sigma_N, \quad (2)$$

where $\Delta\tau$ is the change in shear stress in the direction of slip, $\Delta\sigma_N$ is the change in normal stress (assumed positive in extension), and μ' is the effective coefficient of friction. Positive Coulomb stress changes on a given fault are presumed to push that fault toward failure [*King et al*., 1994; *Stein*, 1999].

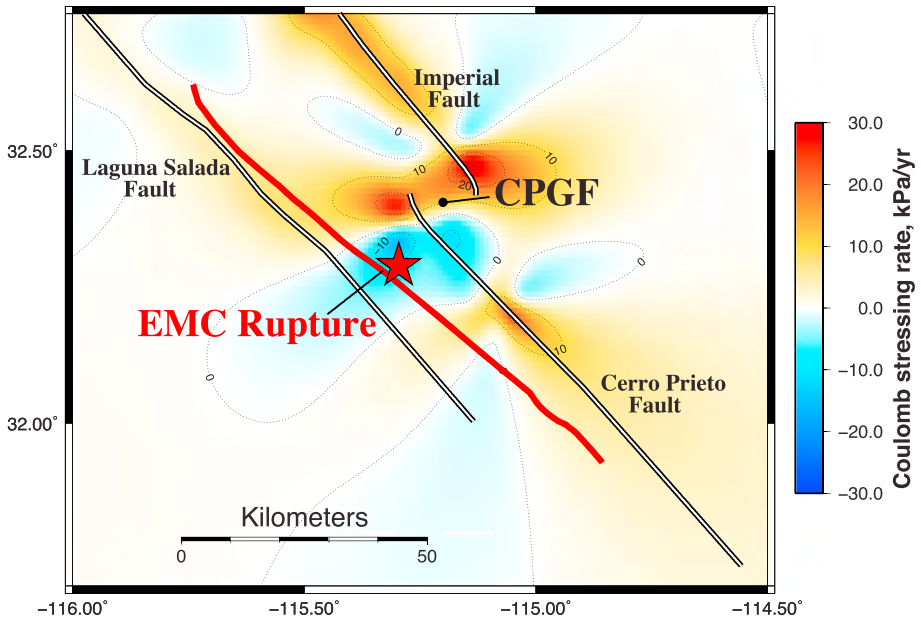

Figure 4. Coulomb stressing rate in the El Mayor-Cucapah (EMC) rupture zone due to tectonic stresses from regional faults [*Smith-Konter and Sandwell*, 2009]. The stress field shown is for right-lateral slip at 5 km depth on vertical faults oriented parallel to the F2 and F3 EMC subevent fault planes (N48°W). The color scale is identical to that of Figure 3.

To compute the Coulomb stresses associated with our fluid extraction model, we first generalize the Fourier-domain approach of *Steketee* [1958] (see Text S1 for details) to obtain the 3-D stress tensor due to an arbitrary distribution of radial point sources imbedded in an elastic half space. We then decompose the local stress tensor into shear and normal components for the fault geometries and slip directions of the subevents that comprise the EMC rupture sequence and compute the local Coulomb stressing rate. We assume typical values for the shear modulus (32 GPa) and effective coefficient of friction of (0.4) [*Lin and Stein*, 2004].

From our model, we estimate that energy production at the CPGF generates a Coulomb stressing rate of ~ +11 kPa/yr at the M_w 4.3 foreshock hypocenter (Figure 3a). This stressing rate is considerable, since Coulomb stress changes as low as 10 kPa have been known to trigger earthquake activity [*Stein*, 1999]. While the foreshock was itself a relatively small event, it occurred in close proximity in both space and time to the hypocenter of the initial F1 main shock subevent, so its role in initiating the main shock event sequence cannot be discounted.

Extraction at the CPGF also caused positive Coulomb stress changes on the faults that ruptured in the EMC main shock. We estimate stressing rates of ~ +12 kPa/yr at the hypocenter of the initial F1 plane (Figure 3b). In contrast to the right-lateral subevents on F2 and F3, the F1 subevent (M_w 6.3) was characterized by mostly normal slip, with the majority of the moment release occurring in the first 10 s of rupture [*Wei et al.*, 2011]. After a near-complete cessation in moment release, the rupture jumped from the F1 fault plane to the steeply dipping F2 and F3 faults striking to the NW. Though the F2 and F3 fault planes extend more than 50 km to the north and south, respectively, their hypocenters were close enough to the CPGF to be influenced by its stress field (Figures 3c and 3d). In fact, the estimated stressing rate of ~ +15 kPa/yr at the F2 hypocenter slightly exceeds the estimate for the stressing rate on F1. We further note that the modeled Coulomb stressing rates on the EMC subevents are caused primarily by increases in extensional stress (Figure S2), which unclamp the fault plane and allow for failure at lower levels of shear stress. Extraction at the CPGF therefore created a favorable environment for the EMC rupture to jump from F1 to F2 and F3, and continue to propagate bilaterally, rather than simply terminate as a smaller event with the cessation of slip on F1.

5. Tectonic Stressing Rates Near the EMC Hypocenter

Our results indicate that stresses from the CPGF may have played a role in stressing the previously latent faults that ruptured in the EMC earthquake. These faults, however, are also subjected to the tectonic stress

field generated by interseismic slip on the deep extents of the nearby regional faults. To assess the effect of the magnitude of the tectonic stress field on the EMC rupture zone, we apply a regional stress accumulation model [*Smith-Konter and Sandwell*, 2009] in which the southern San Andreas Fault system is subdivided into 18 different fault strands, each with its own slip rate and locking depth that are constrained by geologic and geodetic observations. The tectonic stress field in the EMC rupture zone is dominated by the effects of the Imperial (40 mm/yr slip rate and 5.9 km locking depth) and Cerro Prieto (40 mm/yr slip rate and 10 km locking depth) faults and secondarily by the Laguna Salada (5 mm/yr slip rate and 10 km locking depth) fault. We note that this model only provides an estimate of the tectonic stress during the interseismic period, so the long-term loading (i.e., including coseismic effects) of the EMC fault zone by these faults will be somewhat different.

Using this model, we compute the tectonic Coulomb stressing rate on faults striking N48°W, parallel to the EMC rupture trace (Figure 4). The tectonic stressing rate of ~ −8 kPa/yr at the EMC hypocenter is negative, primarily due to fault normal compression (Figure S5) and is smaller in magnitude than the anthropogenic stressing rate from the CPGF. Thus, while regional right-lateral motion must have stressed the EMC faults to near failure over thousands of years prior to the EMC rupture, current interseismic tectonic stressing inhibits the initiation of rupture at the EMC hypocenter. Without the loading from the CPGF over the past 40 years, tectonic forces would have been changing the stress environment on the EMC faults over this time period to be less conducive to rupture.

6. Discussion

Our estimates of positive Coulomb stressing rates in the EMC rupture zone are driven primarily by the increased extensional stresses caused by volumetric contraction in the CPGF production zone. We note, however, that the a priori depth constraint on our model and the inherent uncertainties in the hypocentral depths of the EMC subevents (which are deeper than the production zone) are important sources of uncertainty in our estimates, as is our choice for the effective coefficient of friction on the fault interface, which maps extensional stress changes to Coulomb stress changes (Figures S3 and S4). Furthermore, the Coulomb failure hypothesis is itself an oversimplification of the complex process of earthquake rupture initiation, a fact which precludes the establishment of a causal link between positive Coulomb stressing and the occurrence of any individual earthquake. For these reasons, our estimates of Coulomb stressing rates on the EMC rupture zone should only be interpreted as first-order approximations, and we hesitate to draw definitive conclusions about the role that the CPGF may have played in the EMC rupture sequence.

Our results do, however, demonstrate that fluid extraction at the CPGF causes a substantial perturbation to the regional stress field. The magnitude of the Coulomb stressing rate within the EMC rupture zone depends mainly upon its proximity to the CPGF and the total rate of volume loss within the production zone, and is relatively insensitive to the fine spatial details of the fluid extraction model. It is notable that the magnitude of the estimated anthropogenic stressing in the EMC rupture zone actually exceeds that of the background tectonic stressing rate (and is in fact of opposite sign), in contrast to stressing from ground water pumping in the San Joaquin Valley of California, which is 15 to 150 times smaller in magnitude, yet has been implicated in changes in seismicity on the San Andreas Fault [*Amos et al*., 2014].

Anthropogenic stresses from human activities, including those from reservoir impoundment [*Ge et al*., 2009], wastewater injection at conventional oilfields [*Keranen et al*., 2013], and geothermal energy production [*Deichmann and Giardini*, 2009] have all been directly linked to increased seismicity. Recent studies have found a direct correlation between net fluid extraction and local seismicity at the Salton Sea Geothermal Field [*Brodsky and Lajoie*, 2013], where the rate of net fluid extraction is almost an order of magnitude smaller than that of the CPGF. The *National Research Council* [2013] concluded that maintaining a balance of extracted and injected fluids is essential to limiting the potential for energy production-related induced seismicity. Only 30% of the extracted fluid is reinjected at the CPGF [*Gutiérrez-Negrín et al*., 2010], which stands in contrast to the more balanced reinjection practices at the other geothermal fields in the region [*California Department of Conservation*, 2014]. The CPGF is a vital economic resource, but the influence of its anthropogenic stress field should not be ignored in future seismic hazard assessments of the Valle de Mexicali, home to more than a million people.

Acknowledgments

This material is based upon work supported by the National Science Foundation Graduate Research Fellowship Program (NSFGRFP) under grant 2014176918. Additional support was provided by the NSF EarthScope program (EAR-1147427) and by the Southern California Earthquake (SCEC) grant 14031. The ALOS PALSAR L1.0 data were provided by JAXA through the Alaska Satellite Facility (ASF). This research is also based on data provided by the Plate Boundary Observatory operated by UNAVCO for Earthscope (www.earthscope.org). The figures for this work were generated using the Generic Mapping Toolbox (GMT) [*Wessel et al*., 2013]. We thank P. Shearer for his helpful comments and suggestions and are grateful for the thoughtful reviews provided by R. Burgmann, an anonymous reviewer, and the Associate Editor, all of which greatly improved the manuscript.

The Editor thanks Roland Burgmann and an anonymous reviewer for their assistance in evaluating this paper.

References

Amos, C. B., P. Audet, W. C. Hammond, R. Burgmann, I. A. Johanson, and G. Blewitt (2014), Uplift and seismicity driven by groundwater depletion in central California, *Nature*, *509*, 483–486.

Atwater, T., and J. Stock (1998), Pacific North America plate tectonics of the Neogene southwestern United States: An update, *Int. Geol. Rev.*, *40*, 375–402.

Barnard, F. (1968), Structural geology of the Sierra de los Cucapas, northeastern Baja California, Mexico, and Imperial County, California, PhD thesis, pp. 1–155, Univ. of Colo., Denver.

Bennett, R. A., W. Rodi, and R. E. Reilinger (1996), Global positioning system constraints on fault slip rates in southern California and northern Baja, Mexico, *J. Geophys. Res.*, *101*, 21,943–21,960, doi:10.1029/96JB02488.

Brodsky, E. E., and L. J. Lajoie (2013), Anthropogenic seismicity rates and operational parameters at the Salton Sea Geothermal Field, *Science*, *341*, 543–546.

California Department of Conservation (2014), GeoSteam—Query geothermal well records, production and injection data.

Carnec, C., and H. Fabriol (1999), Monitoring and modeling land subsidence at the Cerro Prieto Geothermal Field, Baja California, Mexico, using SAR interferometry, *Geophys. Res. Lett.*, *26*, 1211–1214, doi:10.1029/1999GL900062.

CFE (2006), Cerro Prieto Geothermal Field (brochure), pp. 1–36, Comisión Federal de Electricidad, Residencia General de Cerro Prieto, México.

Chen, C. W., and H. A. Zebker (2001), Two-dimensional phase unwrapping with use of statistical models for cost functions in nonlinear optimization, *J. Opt. Soc. Am. A*, *18*, 338–351.

Deichmann, N., and D. Giardini (2009), Earthquakes induced by the stimulation of an enhanced geothermal system below Basel (Switzerland), *Seismol. Res. Lett.*, *80*, 784–798.

Fletcher, J. M., and R. M. Spelz (2009), Patterns of Quaternary deformation and rupture propagation associated with an active low-angle normal fault, Laguna Salada, Mexico: Evidence of a rolling hinge?, *Geosphere*, *5*, 385–407.

Fletcher, J. M., et al. (2014), Assembly of a large earthquake from a complex fault system: Surface rupture kinematics of the 4 April 2010 El Mayor-Cucapah (Mexico) *Mw* 7.2 earthquake, *Geosphere*, *10*, 797–827.

Ge, S., M. Liu, N. Lu, J. W. Godt, and G. Luo (2009), Did the Zipingpu Reservoir trigger the 2008 Wenchuan earthquake?, *Geophys. Res. Lett.*, *36*, L20315, doi:10.1029/2009GL040349.

Glowacka, E., and F. A. Nava (1996), Major earthquakes in Mexicali Valley, Mexico, and fluid extraction at Cerro Prieto Geothermal Field, *Bull. Seismol. Soc. Am.*, *86*, 93–105.

Glowacka, E., O. Sarychikhina, and F. Nava (2005), Subsidence and stress change in the Cerro Prieto geothermal field, BC, Mexico, *Pure Appl. Geophys.*, *162*, 2095–2110.

Glowacka, E., O. Sarychikhina, F. Suárez, F. A. Nava, and R. Mellors (2010), Anthropogenic subsidence in the Mexicali Valley, Baja California, Mexico, and slip on the Saltillo fault, *Environ. Earth Sci.*, *59*, 1515–1524.

Gutiérrez-Negrín, L. C. A., R. Maya-González, and J. L. Quijano-León (2010), Current status of geothermics in Mexico, Proceedings World Geothermal Congress, Bali, Indonesia, 25–29 April.

Hanssen, R. F. (2001), *Radar Interferometry: Data Interpretation and Error Analysis*, 328 pp., Kluwer Acad., Dordrecht, Netherlands.

Hauksson, E., J. Stock, K. Hutton, W. Yang, J. Vidal-Villegas, and H. Kanamori (2011), The 2010 *Mw* 7.2 El Mayor-Cucapah earthquake sequence, Baja California, Mexico and Southernmost California, USA: Active seismotectonics along the Mexican Pacific margin, *Pure Appl. Geophys.*, *168*, 1255–1277.

Hauksson, E., W. Yang, and P. M. Shearer (2012), Waveform relocated earthquake catalog for Southern California (1981 to June 2011), *Bull. Seismol. Soc. Am.*, *102*, 2239–2244.

Keranen, K. M., H. M. Savage, G. A. Abers, and E. S. Cochran (2013), Potentially induced earthquakes in Oklahoma, USA: Links between wastewater injection and the 2011 *Mw* 5.7 earthquake sequence, *Geology*, *41*, 699–702.

King, G. C. P., R. S. Stein, and J. Lin (1994), Static stress changes and the triggering of earthquakes, *Bull. Seismol. Soc. Am.*, *84*, 935–953.

Lin, J., and R. S. Stein (2004), Stress triggering in thrust and subduction earthquakes and stress interaction between the southern San Andreas and nearby thrust and strike-slip faults, *J. Geophys. Res.*, *109*, B02303, doi:10.1029/2003JB002607.

Lippmann, M. J., A. H. Truesdell, S. E. Halfman-Dooley, and A. Mañónm (1991), A review of the hydrogeologic-geochemical model for Cerro Prieto, *Geothermics*, *20*, 39–52.

Mogi, K. (1958), Relations between the eruptions of various volcanoes and the deformations of the ground surfaces around them, *Bull. Earthquake Res. Inst. Univ. Tokyo*, *36*, 99–134.

Mossop, A., and P. Segall (1997), Subsidence at The Geysers Geothermal Field, N. California from a comparison of GPS and leveling surveys, *Geophys. Res. Lett.*, *24*, 1839–1842, doi:10.1029/97GL51792.

Mossop, A., and P. Segall (1999), Volume strain within The Geysers geothermal field, *J. Geophys. Res.*, *104*, 29,113–29,131, doi:10.1029/1999JB900284.

National Research Council (2013), *Induced Seismicity Potential in Energy Technologies*, National Academies Press, Washington, D. C.

Ocampo-Díaz, J. D. D., B. Valdez-Salaz, M. Shorr, M. Sauceda, and N. Rosas-González (2005), Review of corrosion and scaling problems in Cerro Prieto geothermal field over 31 years of commercial operations, Proceedings of World Geothermal Congress, International Geothermal Association (IGA), Antalya, Turkey.

Sarychikhina, O. (2003), *Modelación de Subsidencia en el Campo Geotérmico Cerro Prieto*, pp. 1–101, Centro de Investigación Científica y Educación Superior de Ensenada, Ensenada, Mexico.

Sarychikhina, O., E. Glowacka, R. Mellors, and F. S. Vidal (2011), Land subsidence in the Cerro Prieto Geothermal Field, Baja California, Mexico, from 1994 to 2005: An integrated analysis of DInSAR, leveling and geological data, *J. Volcanol. Geotherm. Res.*, *204*, 76–90.

Segall, P. (2010), *Earthquake and Volcano Deformation*, 430 pp., Princeton Univ. Press, Princeton, N. J.

Sieh, K. (1993), Near-field investigations of the Landers earthquake sequence, April to July 1992, *Science*, *260*, 171–176.

Smith-Konter, B., and D. Sandwell (2009), Stress evolution of the San Andreas fault system: Recurrence interval versus locking depth, *Geophys. Res. Lett.*, *36*, L13304, doi:10.1029/2009GL037235.

Stein, R. S. (1999), The role of stress transfer in earthquake occurrence, *Nature*, *402*, 605–609.

Steketee, J. A. (1958), On Volterra's dislocations in a semi-infinite elastic medium, *Can. J. Phys.*, *36*, 192–205.

Vasco, D. W., C. Wicks, K. Karasaki, and O. Marques (2002), Geodetic imaging: Reservoir monitoring using satellite interferometry, *Geophys. J. Int.*, *149*, 555–571, doi:10.1046/j.1365-246X.2002.01569.x.

Wei, S., et al. (2011), Superficial simplicity of the 2010 El Mayor-Cucapah earthquake of Baja California in Mexico, *Nat. Geosci.*, *4*, 615–618.

Wessel, P., W. H. F. Smith, R. Scharroo, J. Luis, and F. Wobbe (2013), Generic mapping tools: Improved version released, *Eos Trans. AGU*, *94*, 409–410, doi:10.1002/2013EO450001.

Auxiliary Material for

Did Stresses From the Cerro Prieto Geothermal Field Influence the El Mayor-Cucapah Rupture Sequence?

Daniel T. Trugman[1*], Adrian A. Borsa[1], David T. Sandwell[1]

1: Institute for Geophysics and Planetary Physics, Scripps Institution of Oceanography, La Jolla, California, USA

*Corresponding Author. Address: Daniel T. Trugman, Scripps Institution of Oceanography, UC San Diego, 9500 Gilman Drive - 0225, La Jolla, CA, 92037-0225. Email: dtrugman@ucsd.edu

Introduction

This Auxiliary Material includes contains three primary components: Supplementary Text (with associated references), Supplementary Data Set 1, and Supplementary Figures S1 through S5 (with associated captions). The Supplementary Text details the methodology in this study related to: (1) InSAR observations, (2) our fluid extraction model, and (3) Coulomb stress computations. Supplementary Data Set 1 contains our preferred Mogi source fluid extraction model in a column-formatted text file (longitude, latitude, depth, and source volume change/year). Figures S1 through S5 detail the vertical subsidence rate near the Cerro Prieto Geothermal Field (S1), decompose the

Coulomb stress into shear and normal stress components (S2 for the fluid extraction model and S5 for the regional tectonic model), and display the results of our sensitivity analyses for hypocentral depth (S3) and effective coefficient of friction (S4).

Supplementary Text

1. InSAR Observations

We use Advanced Land Observing Satellite (ALOS) InSAR data acquired from 2006-2009 to study in detail the surface subsidence at the Cerro Prieto Geothermal Field (CPGF) immediately preceding the El Mayor-Cucapah (EMC) event. The ALOS L-band radar achieves better temporal coherence in vegetated areas than does the C-band radar on satellites such as Envisat [*Sandwell et al.,* 2008] , allowing for improved phase estimates in the vegetated regions near the CPGF [*Glowacka et al.,* 2005] . All InSAR data were processed using the GMTSAR software package [*Sandwell et al.,* 2011] , using the digital elevation model from the Shuttle Radar Topography Mission (SRTM) to remove the topographic phase [*Farr et al.,* 2007] . We use the SNAPHU algorithm [*Chen and Zebker,* 2001] to unwrap the phase of individual interferograms.

The InSAR image of the line-of-sight (LOS) surface velocity (Figure 2a) was generated by stacking two unwrapped ALOS interferograms. We initially processed 16 images along descending Track 211 and 7 images along ascending Track 532, but only used 4 of the T532 images where the phase unwrapping over the geothermal area was complete. These were 2-year interferograms (year 2006, day 309 to year 2008, day 315; year 2007, day 036 to year 2009, day 041). Because the subsidence rate in the area is very large, our selection process was based on phase continuity. The ascending and

descending interferograms showed similar patterns, suggesting mainly vertical deformation in the region, in agreement with previous studies [*Sarychikhina,* 2003; *Glowacka et al.,* 2005; *Sarychikhina et al.,* 2011] .

2. Fluid Extraction Model

We model fluid extraction at the CPGF as a lateral distribution of finely-spaced Mogi pressure sources at constant depth. This approach allows us to vary the source intensity on a fine spatial scale to better capture the complex spatial patterns of extraction, injection, and recharge beneath the CPGF. We position the center of the source distribution in the production zone of the CPGF (-115.20ºE, 32.1ºN) and at the mean production depth of 2.7 km [*Lippmann et al.,* 1991; *Gutiérrez-Negrín et al.,* 2010] . We discretize the source distribution using a single horizontal layer with a grid-spacing of 0.5 km in both lateral directions for a total of 436 evenly-spaced sources.

We invert for the source intensities using the InSAR observations of LOS surface velocities. For a single Mogi source at position (x_0, y_0, z_0 <0) within an elastic halfspace (Poisson's ratio υ), the displacement vector (u_x , u_y , u_z) at surface position (x, y, z = 0), can be written as

$$\begin{pmatrix} u_x \\ u_y \\ u_z \end{pmatrix} = \frac{(1-\upsilon)\Delta V}{\pi} \begin{pmatrix} (x-x_0)/R^3 \\ (y-y_0)/R^3 \\ (-z_0)/R^3 \end{pmatrix} \qquad (S1)$$

where $R = \sqrt{(x-x_0)^2 + (y-y_0)^2 + (-z_0)^2}$ is the distance from the source to the surface observation point and ΔV is the associated volume change (i.e., the source intensity) [*Segall,* 2010] . Subsidence requires $\Delta V < 0$.

The observed surface deformation is the superposition of the deformation caused by each individual Mogi source in the distribution. If the source positions are known, then the forward computation of the LOS velocity field can be written in the form:

$$\boldsymbol{d} = \underline{\boldsymbol{G}}\,\boldsymbol{m} \quad , \tag{S2}$$

where $\boldsymbol{d}$ is the data vector of observed LOS velocities (the dot product of the displacement velocity vector and satellite look vector)**,** $\boldsymbol{m}$ is the model vector of source volumes, and $\underline{\boldsymbol{G}}$ is the matrix of LOS displacement Green's functions derived from equation (1). We invert for the source volumes by performing a regularized least-squares inversion (e.g., [*Parker,* 1994]):

$$\boldsymbol{m_0} = \operatorname{argmin}\left\{\left\|\boldsymbol{d} - \underline{\boldsymbol{G}}\boldsymbol{m}\right\|^2 + \lambda^2\left\|\underline{\boldsymbol{D}}\boldsymbol{m}\right\|^2\right\}, \tag{S3}$$

to obtain the model $\boldsymbol{m}_0$ that minimizes a linear combination of: (i) the residual norm between the observed (InSAR-derived) and model-predicted LOS velocity, and (ii) a model norm parameterized by a first-order Tikhonov smoothing operator $\underline{\boldsymbol{D}}$. We chose a smoothing parameter of 10^{-6} by examining trade-off curves of the residual and model norm. We supply our preferred model (longitude, latitude, depth, and source volume change/year) in Supplementary Data Set 1. We also performed analogous inversions with 3 and 5 horizontal layers, and with grid spacings ranging from 0.25 km to 2.5 km, and observed no appreciable change to the data misfit or modeled integrated volume loss. The addition of multiple layers tends to destabilize the inversion process, so our preferred model contains a single horizontal layer.

3. Coulomb Stress Computations

Given a fault plane orientation (parameterized in terms of a normal and slip vector), we define the Coulomb stress change as

$$\Delta\sigma_C = \Delta\tau + \mu'\Delta\sigma_N \,, \qquad (S4)$$

where $\Delta\tau$ is the change in shear stress in the direction of slip, $\Delta\sigma_N$ is the change in normal stress (assumed positive in extension), and μ' is the effective coefficient of friction. Positive Coulomb stress changes on a given fault are presumed to push that fault toward failure [*King et al.,* 1994; *Stein,* 1999] , and are caused by increases in shear stress or extensional normal stress (i.e., unclamping of the fault plane). For the stress computations in this study, we assume a homogenous elastic medium with a shear modulus of 32 GPa, Poisson's ratio of 0.25, and an effective coefficient of friction of 0.4 [*Lin and Stein,* 2004] .

To compute the Coulomb stresses associated with our fluid extraction model, we first generalize the Fourier-domain approach of *Steketee* [1958] to obtain the Green's function for a radial point source in an elastic half-space. In this formulation, the half-space Green's function is a semi-analytic function of the horizontal wavenumbers (k_x and k_y) and vertical position (z). This half-space Green's function is composed of the superposition of three terms: (i) the full-space Green's function for a source at depth $z = -a$, (ii) an image full-space Green's function a $z = +a$, and (iii) a Boussinesq correction to ensure zero traction at the free surface ($z = 0$).

With the half-space Green's function in hand, the full 3D strain tensor for an arbitrary distribution of radial point sources is easily obtained through convolution (multiplication in the wavenumber domain) of the Green's function and source distribution. To compute Coulomb stresses, we apply assume isotropic, linear elasticity to convert strains into stresses, and then resolve the local stress tensor on the fault plane geometries (and slip directions) of each of the individual subevents that comprise the

EMC rupture sequence. For EMC subevents F1 through F3, we use the fault plane parameterization (strike, dip, and rake) presented in *Wei et al.* [2011] to obtain the slip and normal vectors. For the M_w 4.3 foreshock, we use the fault plane and slip orientation described by *Hauksson et al.* [2011].

To assess the effect of the magnitude of the tectonic stress field on the EMC rupture zone, we apply the regional stress-accumulation model [Smith-Konter and Sandwell, 2009] described in the main text. We then compute the normal, shear and Coulomb tectonic stressing rates at 5 km depth on faults striking N48W, parallel to the EMC rupture trace (Figures 4 and S5).

References

Chen, C. W. and H. A. Zebker (2001), Two-dimensional phase unwrapping with use of statistical models for cost functions in nonlinear optimization*, JOSA A, 18*, 338-351, doi: 10.1364/JOSAA.18.000338.

Farr, T. G. et al. (2007), The Shuttle Radar Topography Mission*, Rev. Geophys., 45*, -RG2004, doi: 10.1029/2005RG000183.

Glowacka, E., O. Sarychikhina, and F. Nava (2005), Subsidence and stress change in the Cerro Prieto geothermal field, BC, Mexico*, Pure Appl. Geophys., 162*, 2095-2110, doi: 10.1007/s00024-005-2706-7.

Gutiérrez-Negrín, L. C. A., R. Maya-González, and J. L. Quijano-León (2010), Current Status of Geothermics in Mexico, Proceedings World Geothermal Congress, Bali, Indonesia, 25-29 April, 2010.

133 Hauksson, E., J. Stock, K. Hutton, W. Yang, J. Vidal-Villegas, and H. Kanamori (2011),
134 The 2010 Mw 7.2 El Mayor-Cucapah Earthquake Sequence, Baja California,
135 Mexico and Southernmost California, USA: Active Seismotectonics along the
136 Mexican Pacific Margin, *Pure Appl. Geophys., 168*, 1255-1277, doi:
137 10.1007/s00024-010-0209-7.
138 King, G. C. P., R. S. Stein, and J. Lin (1994), Static stress changes and the triggering of
139 earthquakes, *Bull. Seismol. Soc. Am., 84*, 935-953.
140 Lin, J. and R. S. Stein (2004), Stress triggering in thrust and subduction earthquakes and
141 stress interaction between the southern San Andreas and nearby thrust and strike-
142 slip faults, *J. Geophys. Res.: Solid Earth (1978–2012), 109*, doi:
143 10.1029/2003JB002607.
144 Lippmann, M. J., A. H. Truesdell, S. E. Halfman-Dooley, and M. A. (1991), A review of
145 the hydrogeologic-geochemical model for Cerro Prieto, *Geothermics, 20*, 39-52,
146 doi: 10.1016/0375-6505(91)90004-F.
147 Parker, R. L. (1994), *Geophysical Inverse Theory*, 386 pp., Princeton University Press,
148 Princeton, New Jersey.
149 Sandwell, D. T., D. Myer, R. Mellors, M. Shimada, B. Brooks, and J. Foster (2008),
150 Accuracy and Resolution of ALOS Interferometry: Vector Deformation Maps of
151 the Father's Day Intrusion at Kilauea, *Geoscience and Remote Sensing, IEEE*
152 *Transactions on, 46*, 3524-3534, doi: 10.1109/TGRS.2008.2000634.
153 Sandwell, D., R. Mellors, X. Tong, M. Wei, and P. Wessel (2011), Open radar
154 interferometry software for mapping surface deformation, *Eos, Transactions*
155 *American Geophysical Union, 92*, 234-234, doi: 10.1029/2011EO280002.

156 Sarychikhina, O. (2003), Modelación de subsidencia en el campo geotérmico Cerro
157 Prieto, 1-101 pp., Centro de Investigación Científica y Educación Superior de
158 Ensenada, Ensenada, Mexico.
159 Sarychikhina, O., E. Glowacka, R. Mellors, and F. S. Vidal (2011), Land subsidence in
160 the Cerro Prieto Geothermal Field, Baja California, Mexico, from 1994 to 2005:
161 An integrated analysis of DInSAR, leveling and geological data, *J. Volcanol.*
162 *Geotherm. Res., 204*, 76-90, doi: 10.1016/j.jvolgeores.2011.03.004.
163 Segall, P. (2010), *Earthquake and Volcano Deformation*, 430 pp., Princeton University
164 Press, Princeton, NJ.
165 Stein, R. S. (1999), The role of stress transfer in earthquake occurrence, *Nature, 402*,
166 605-609, doi: 10.1038/45144.
167 Steketee, J. A. (1958), On Volterra's dislocations in a semi-infinite elastic medium, *Can.*
168 *J. Phys., 36*, 192-205, doi: 10.1139/p58-024.
169 Wei, S. et al. (2011), Superficial simplicity of the 2010 El Mayor-Cucapah earthquake of
170 Baja California in Mexico, *Nat. Geosci., 4*, 615-618, doi: 10.1038/ngeo1213.
171

Supplementary Data Set 1

Supplementary Data Set 1 contains our preferred Mogi source fluid extraction model in a column-formatted text file. Each line of the text file contains the longitude (degrees E), latitude (degrees N), depth (2.7 km for our preferred model), and rate of source volume change (m^3/yr). There are 436 lines in total – one for each Mogi source in the planar distribution.

Supplementary Figures

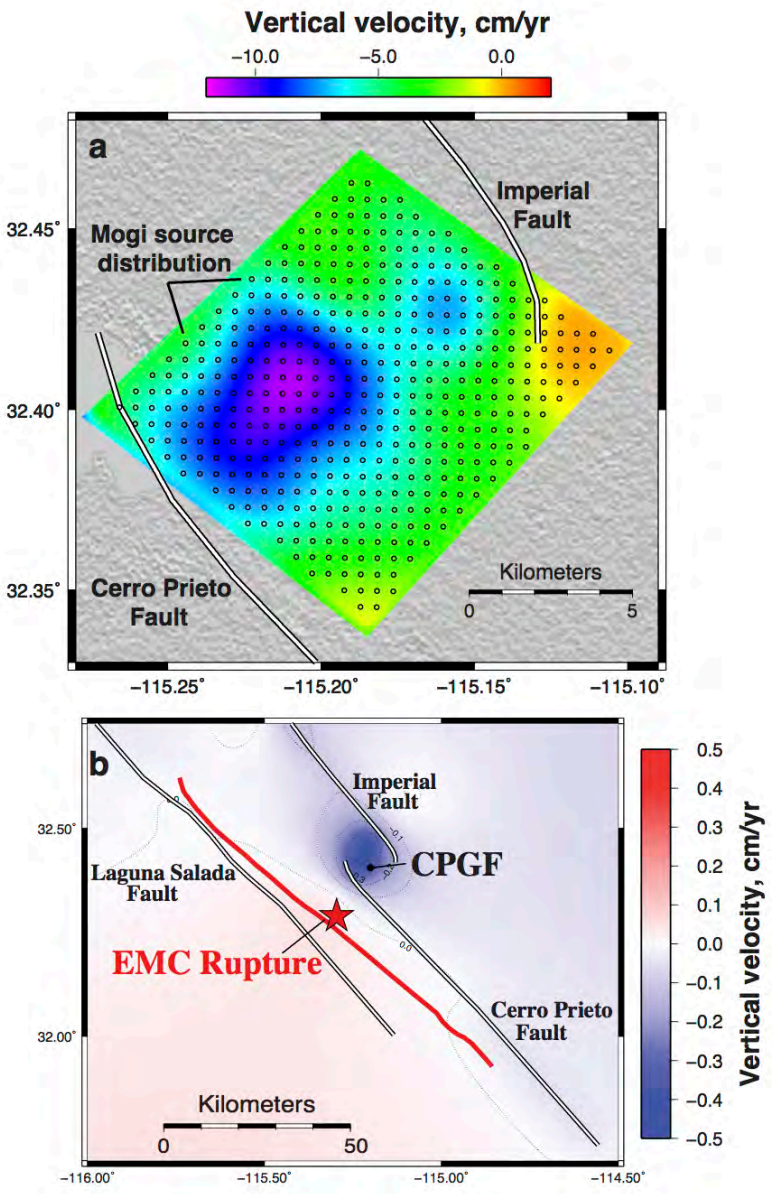

Figure S1. Modeled and tectonic subsidence near the Cerro Prieto Geothermal Field (CPGF). **(a)** Rate of vertical surface subsidence near the CPGF predicted by our preferred Mogi source distribution fluid extraction model. The maximum rate of vertical surface subsidence is ~ 14 cm/year. **(b)** Estimated rate of vertical surface subsidence in the El Mayor-Cucapah (EMC) rupture zone due to natural, interseismic deformation from regional faults. The tectonic subsidence rate was computed using the stress accumulation model of *Smith-Konter and Sandwell* [2009]. The estimated tectonic subsidence rate of 0.4 cm/year within the CPGF is ~ 3% of the observed rate, which is dominantly anthropogenic in origin.

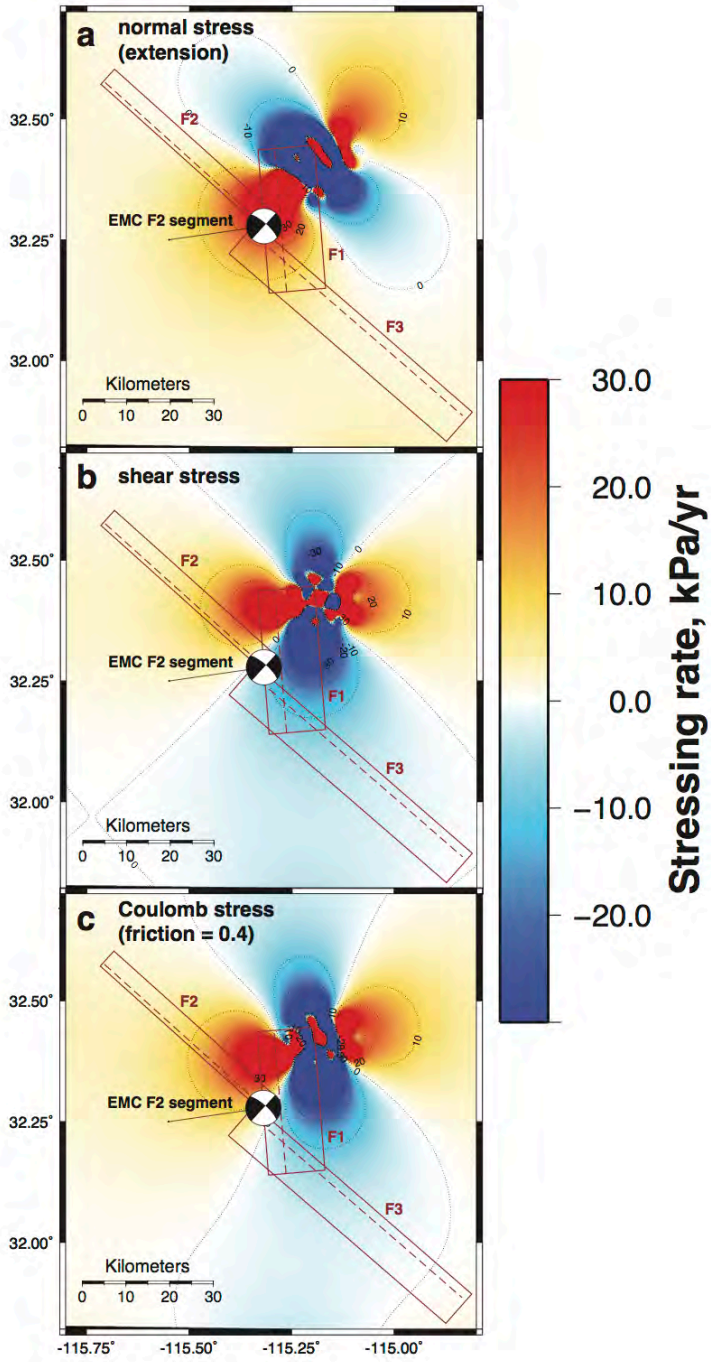

193

194 **Figure S2**. Comparison of **(a)** normal, **(b)** shear, and **(c)** Coulomb stressing rates on El

195 Mayor-Cucapah (EMC) fault plane F2, due to fluid extraction at the Cerro Prieto

196 Geothermal Field. The stressing rates are computed at 5 km depth for the fault geometry

of the EMC F2 subevent (strike = 312°, dip = 75°, rake = -180°). An effective coefficient of friction of 0.4 is assumed for panel c). The stress decomposition for fault plane F3 is nearly identical (as the fault geometry is close to the same). The stress decomposition for F1 is also quite similar, but the extensional stress is slightly reduced (but still positive) at the F1 hypocenter, and the shear stress is also positive at the hypocenter. This difference is due to the difference in fault geometry and slip orientation, as F1 is a normal faulting event with slightly different strike and dip than F2 (a strike-slip event).

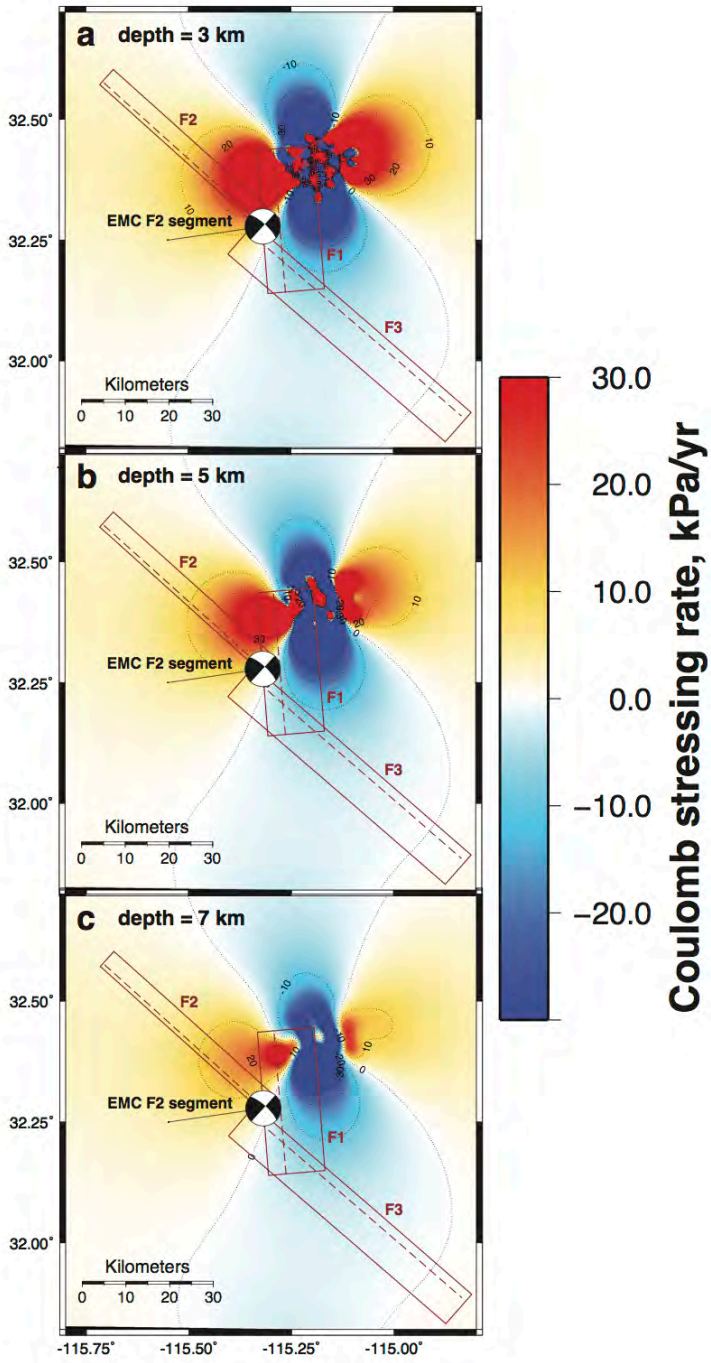

204

205 **Figure S3**. Sensitivity analysis of hypocentral depth for Coulomb stressing rate on El

206 Mayor-Cucapah (EMC) fault plane F2 due to fluid extraction at the Cerro Prieto

207 Geothermal Field. An effective coefficient of friction of 0.4 is used for all panels.

208 Modeled Coulomb stressing rate for the fault geometry of the EMC F2 subevent (strike =
209 312°, dip = 75°, rake = -180°**)** at: (**a**) 3 km depth, (**b**) 5 km depth, and (**c**) 7 km depth. The
210 results of this study assume hypocentral depths of 5 km [*Wei et al.,* 2011], and are similar
211 for fault planes F1 and F3 (not shown here).

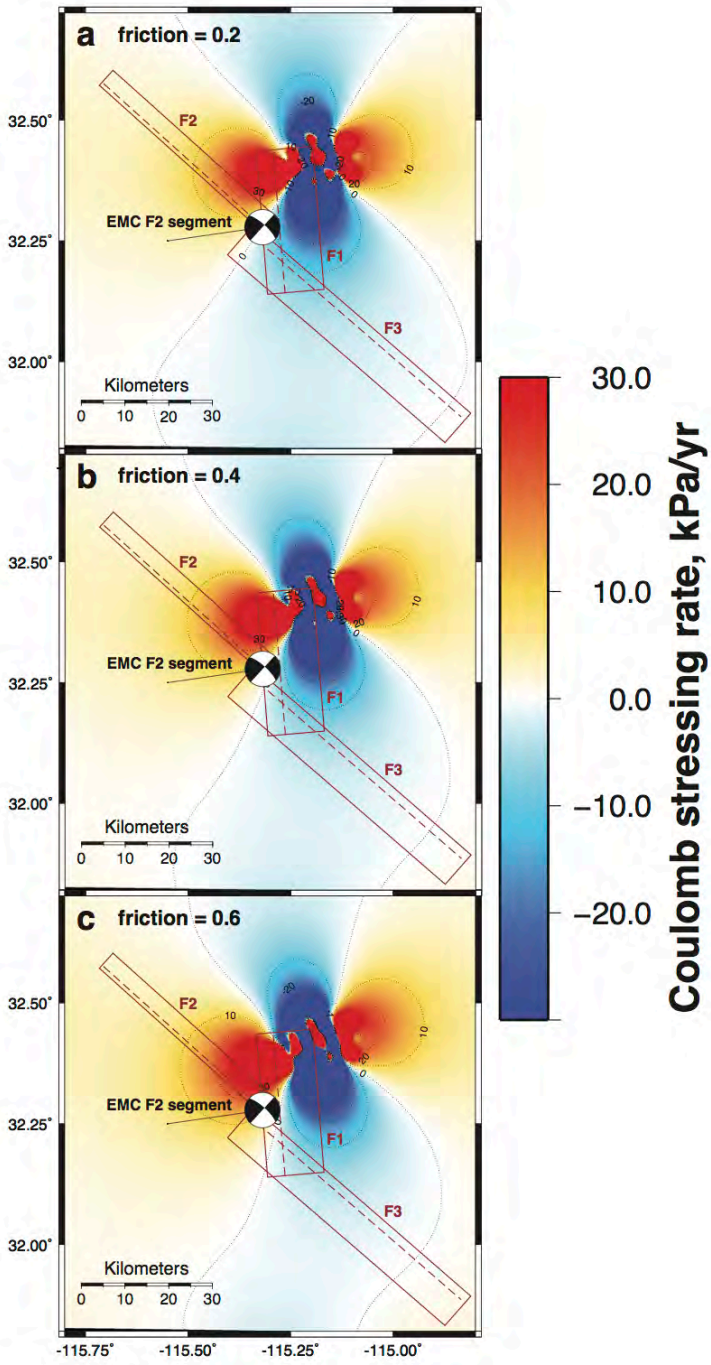

212

213 **Figure S4**. Sensitivity analysis of the effective coefficient of friction for the Coulomb

214 stressing rate on El Mayor-Cucapah (EMC) fault plane F2 due to fluid extraction at the

215 Cerro Prieto Geothermal Field. Modeled Coulomb stressing rate at 5 km depth for the

fault geometry of the EMC F2 subevent (strike = 312°, dip = 75°, rake = -180°**)** assuming: (**a**) an effective coefficient of friction of 0.2, (**b**) an effective coefficient of friction of 0.4, and (**c**) an effective coefficient of friction of 0.6. The results of this study assume an effective coefficient of friction of 0.4, and are similar for fault planes F1 and F3 (not shown here).

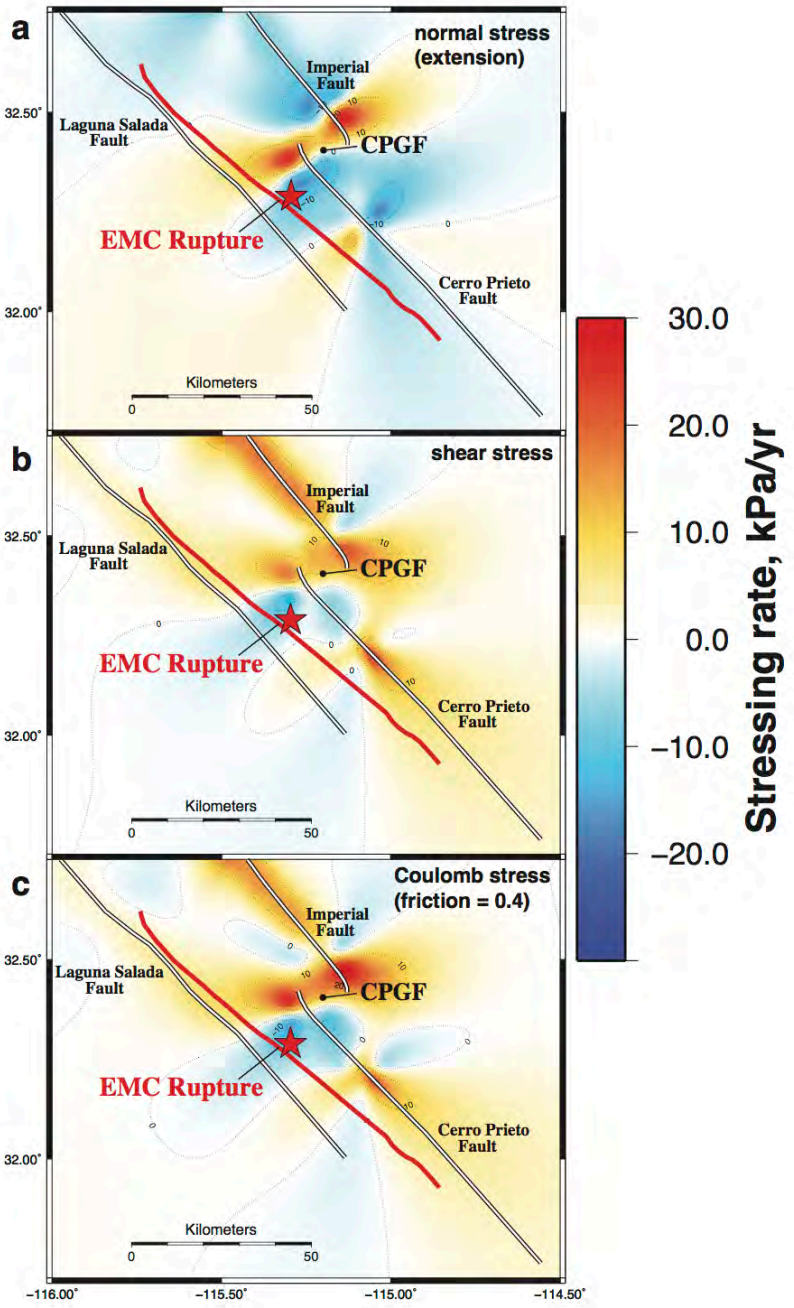

Figure S5. Comparison of **(a)** normal, **(b)** shear, and **(c)** Coulomb stressing rates in the El Mayor-Cucapah (EMC) rupture zone due to tectonic stresses from regional faults [*Smith-Konter and Sandwell,* 2009]. The stress fields shown are for right-lateral slip at 5 km

225 depth on vertical faults oriented parallel to the F2 and F3 EMC subevent fault planes

226 (N48W). An effective coefficient of friction of 0.4 is assumed for panel c).